Journal of
Marine Science
and Engineering

MDPI

Article

Numerical Prediction of Cavitation Fatigue Life and Hydrodynamic Performance of Marine Propellers

Xiaohui Zhang [1,2], Qimao Xu [1], Meng Zhang [1,2,*] and Zhongliang Xie [3]

[1] Yantai Research Institute, Harbin Engineering University, Yantai 265502, China; xh_zhang@hrbeu.edu.cn (X.Z.); xuqimao1568193628@163.com (Q.X.)
[2] College of Shipbuilding Engineering, Harbin Engineering University, Harbin 150001, China
[3] Department of Engineering Mechanics, Northwestern Polytechnical University, Xi'an 710072, China; zlxie@nwpu.edu.cn
* Correspondence: zhangmeng@hrbeu.edu.cn

Abstract: With the increasing stringency of the Energy Efficiency Design Index (EEDI) requirements, improving the efficiency of the propeller has emerged as a significant challenge in the development of eco-friendly ships. Cavitation inevitably occurs, and it reduces the hydrodynamic performance of the propeller and erodes the blade surface, leading to increased fuel consumption. Therefore, reducing cavitation is crucial for ships to meet the EEDI requirement. This paper investigates the fatigue life and hydrodynamic performance of the propeller under different cavitation numbers and speeds. The relationship between propeller fatigue life and propulsion efficiency under cavitation conditions is explored. In simulation, the Schnerr–Sauer theoretical model is employed as the cavitation model. The nominal stress method (*S-N* method) is used to calculate the blade fatigue strength. The KP957 propeller is taken as the research object. The hydrodynamic performance of the propellor under different cavitation numbers is studied by means of the finite volume method. The surface pressure and wall shear stress of the blade within the cycle are calculated, and they are conveniently loaded in the dynamic process to calculate the stress and strain of the propeller using the finite element method. Subsequently, the fatigue life of the propeller is determined based on the *S-N* curve of the blade material. The validity of the study is established by comparing the cavitation results with the experimental results from the Korean Ocean Engineering Research Institute (KORDI) for the KS1295 ship at a speed of 15.7 knots, where the cavitation number in the wake field is 2.5553, and a good consistency is obtained. The findings emphasize the significant impact of cavitation on blade service life and vibration.

Keywords: propeller; cavitation; hydrodynamic performance; fatigue life; fluid-structure interaction

Citation: Zhang, X.; Xu, Q.; Zhang, M.; Xie, Z. Numerical Prediction of Cavitation Fatigue Life and Hydrodynamic Performance of Marine Propellers. *J. Mar. Sci. Eng.* **2024**, *12*, 74. https://doi.org/10.3390/jmse12010074

Academic Editor: Ebrahim Kadivar

Received: 20 November 2023
Revised: 25 December 2023
Accepted: 25 December 2023
Published: 28 December 2023

1. Introduction

In the field of international shipping, ultra-large vessels are deemed as cost-effective maritime freight carriers due to their favorable energy consumption ratios. Nevertheless, as ship tonnage and speed increase, the strain on the ship's propellers becomes more severe, leading to cavitation in the propeller blades. Cavitation in propellers has negative consequences, including increased noise, vibrations, and potential blade damage [1]. This cavitation erosion not only jeopardizes the integrity of the propeller but also results in an increase in surface roughness [2]. As a result, propeller performance declines, and in severe cases, significant damage may occur, adversely affecting normal navigation. Therefore, there is a need to analyze propeller cavitation prediction and assess the fatigue strength under cavitation conditions.

In recent years, there has been a significant increase in research focusing on propeller cavitation performance, particularly through the utilization of numerical simulation methods based on viscous flow. The Reynolds-Averaged Navier-Stokes (RANS) method has gained widespread adoption. Researchers have made innovative advancements in this area. For example, Chowdhury et al. [3] combined the $k - \omega$ SST turbulence model with curvature correction and the Zwart cavitation model to enhance the cavitation prediction accuracy. Long et al. [4] applied $k - \omega$ SST along with the Zwart cavitation model to explore cavitation, vorticity distribution, and particle trajectories of the propeller in the wake of the ship. Although the predicted cavitation shape closely matched experimental results, the cavitation area was slightly larger. Paik et al. [5] utilized FLUENT software 14 and the Schnerr–Sauer cavitation model to achieve more reliable insights into propeller cavitation morphology and hull pulsation pressure. Yilmaz et al. [6] employed the large eddy simulation method with commercial STAR-CCM+ software (2018) and the Schnerr–Sauer cavitation model to investigate ship-propeller-rudder interaction under tip vortex cavitation, showcasing the predictive capabilities of STAR-CCM+. Rizk et al. [7] successfully simulated cavitation flow around the propeller. Zheng et al. [8] simulated unsteady propeller cavitation at the stern using the unsteady RANS method based on OpenFOAM. Lloyd et al. [9] conducted numerical simulations of tip vortex cavitation for the E779A propeller using the RANS and DDES (Delayed-Detached Eddy Simulation) methods. They identified the tip vortex region based on the dimensionless Q-criterion for one of the blades. They found that the combination of the DDES method and the adaptive mesh method is able to significantly reduce the minimum pressure coefficient in the center of the tip vortex. Based on the analysis and comparison of the literature [6–9], It can be concluded that different turbulent simulation methods have a significant impact on the numerical simulation accuracy of tip vortex cavitation of propellers, but the mesh resolution has an even greater impact. It is important to note that the current propeller cavitation prediction often overlooks the impact of deformation, and research on the fatigue life of the propeller under cavitation remains limited.

As a propeller operates underwater, it experiences periodic bubble generation and collapse on its blades, resulting in impact loads on the blade surface [10]. The rotation process of the propeller generates periodic unsteady dynamic loads on the blade surface [11], causing significant variations in surface load distribution in different media such as gas and liquid. Additionally, at higher propeller speeds, the frequency of alternating changes in blade stress becomes too rapid. The continuous action of these alternating loads affects the strength and fatigue life of the blades, directly impacting the operational safety of the propeller. Therefore, propeller design should take into account cavitation factors, which can increase the service life and safety of the propeller [12,13].

For the calculation of propeller fatigue strength, it is essential to determine the varying hydrodynamic load on the propeller blade throughout its rotation cycle. This load serves as the external input for calibrating the propeller blade's strength. Typically, the hydrodynamic load is transferred between the fluid mesh and the structural mesh by integrating the finite element model, material properties, and boundary constraints of the propeller. The stresses and deformations of the propeller blade are then extracted from the results of the finite element method for fatigue analysis. The fluid-structure interaction method, widely employed in various fields to study fatigue characteristics [14–16], plays a crucial role. Regarding the fatigue strength calculation of the propeller under cavitation, the propeller blade's fatigue strength falls into the category of high circumferential fatigue problems due to cyclic loading and high rotational speed [17]. The specification lacks a corresponding fatigue analysis formula. Structural fatigue strength analysis methods include the nominal stress method [18], the junction stress method [19], the local stress method [20], and the fracture mechanics method [21]. The nominal stress method is primarily used in engineering to estimate the effective fatigue life with Finite Element Method (FEM) based on the material's *S-N* curves and fatigue damage accumulation theory [22].

In light of these considerations, this paper establishes a method for predicting propeller cavitation and assessing fatigue life based on Computational Fluid Dynamics (CFD) and Finite Element Method (FEM). We assess the blade strength of the propeller under different cavitation numbers and identify the stress danger areas of the blade. However, we acknowledge that we have not considered the impact of cavitation collapses on stress and propeller life. Additionally, we employ the *S-N* curve of the blade material to evaluate the fatigue life of the propeller model. The findings offer valuable insights into the changing patterns of propeller fatigue strength and hydrodynamic forces under different cavitation numbers. This study could serve as a valuable reference for the development of criteria for propeller cavitation, strength calibration, and discrimination.

2. Mathematical Descriptions

2.1. Governing Equations

This study uses CFD software STARCCM+ V2302(18.02) for numerical simulation. The numerical simulation is based on the theory of viscous fluid mechanics. The fluid is incompressible, and the governing equation includes the continuity equation and the momentum equation:

$$\frac{\partial \rho}{\partial t} + \frac{\partial(\rho u_i)}{\partial x_i} = 0, i = 1,2,3 \tag{1}$$

$$\rho\left[\frac{\partial u_i}{\partial t} + \frac{\partial\left(\overline{u_i u_j}\right)}{\partial x_j}\right] = -\frac{\partial p}{\partial x_i} + \frac{\partial}{\partial x_j}\left[\mu\left(\frac{\partial u_i}{\partial x_j} + \frac{\partial u_j}{\partial x_i} - \frac{2}{3}\delta_{ij}\frac{\partial u_i}{\partial x_i}\right)\right] + \frac{\partial}{\partial x_j}\left(-\rho\overline{u_i' u_j'}\right) \quad i,j = 1,2,3 \tag{2}$$

where u_i and u_j are the velocities of the fluid in i and j directions, respectively, x_i is the coordinate, ρ is the density, p is the pressure, t is the physical time, μ is the dynamic viscosity, δ is the Kronecker delta; $-\rho\overline{u_i' u_j'}$ is the Reynolds stress tensor based on the Boussinesq hypothesis.

The SST $k-\omega$ turbulence model is adopted, which employs the $k-\omega$ and $k-e$ model in the near-wall region and far-field, respectively. The transport equations for the SST $k-\omega$ model are expressed as:

$$\frac{\partial}{\partial t}(\rho k) + \frac{\partial}{\partial x_i}(\rho k u_i) = \frac{\partial}{\partial x_j}\left(\Gamma_k \frac{\partial k}{\partial x_j}\right) + G_k - Y_k \tag{3}$$

$$\frac{\partial}{\partial t}(\rho \omega) + \frac{\partial}{\partial x_i}(\rho \omega u_i) = \frac{\partial}{\partial x_j}\left(\Gamma_\omega \frac{\partial \omega}{\partial x_j}\right) + G_\omega - Y_\omega + D_\omega \tag{4}$$

where Γ_k and Γ_w are the effective diffusivity of k and ω, respectively. G_k and G_w represent the generation of k and ω, respectively. Y_k and Y_w are the dissipation of k and ω, respectively. D_w is the cross-diffusion term.

2.2. Schnerr–Sauer Cavitation Model

Cavitation is an intricate hydrodynamic occurrence. In numerical simulations, the cavitation formation process can be distilled as follows: owing to alterations in local static pressure caused by liquid flow, when the local pressure falls below the liquid's saturated vapor pressure, minuscule gas nuclei in the liquid explosively vaporize, giving rise to bubbles. To calculate the mass transition between vapor and liquid, it is essential to establish a model capturing the relationship between the two phases, commonly referred to as the cavitation model. The Schnerr–Sauer cavitation model [23] is a simplified rendition of the more comprehensive Rayleigh–Plesset equation, neglecting the influences of cavitation growth acceleration, as well as viscous effects and surface tension effects. Given that the impacts of fluid viscosity and surface tension are typically disregarded in practical engineering applications, the Schnerr–Sauer cavitation model proves suitable for addressing the majority of engineering scenarios.

The transport equation for the vapor phase mass fraction is as follows:

$$\frac{\partial(\rho \alpha_v)}{\partial t} + \frac{\partial(\rho u_i \alpha_v)}{\partial x_i} = \dot{m}_c + \dot{m}_v \tag{5}$$

where α_v is the gas phase volume fraction; ρ_v is the gas density; $\dot{m}_c$ and $\dot{m}_v$ are the mass expressions for the condensation and vaporization mass exchange processes, respectively.

In the Schnerr-Sauer model, $\dot{m}_c$ and $\dot{m}_v$ are expressed as

$$\dot{m}_c = C_c \frac{3\rho_v \rho_1 \alpha_v (1-\alpha_v)}{\rho R} \mathrm{sgn}(P_v - P) \sqrt{\frac{2|P_v - P|}{3\rho_1}} \tag{6}$$

$$\dot{m}_v = C_v \frac{3\rho_v \rho_1 \alpha_v (1-\alpha_v)}{\rho R} \mathrm{sgn}(P_v - P) \sqrt{\frac{2|P_v - P|}{3\rho_1}} \tag{7}$$

where C_c and C_v are empirical coefficients; ρ_1 is the density of the liquid; ρ_v is the saturated vapor pressure at the corresponding temperature; P is the local pressure; and R is the average radius of the cavitation.

The propeller's advance coefficient J, thrust coefficient K_T, torque coefficient K_Q, open water efficiency η_0 and cavitation number σ_n are expressed as follows:

$$J = \frac{V}{nD} \tag{8}$$

$$K_T = \frac{T}{\rho n^2 D^4} \tag{9}$$

$$K_Q = \frac{Q}{\rho n^2 D^5} \tag{10}$$

$$\eta_0 = \frac{J}{2\pi} \frac{K_T}{K_Q} \tag{11}$$

$$\sigma_n = \frac{p_0 - p_v}{0.5\rho (nD)^2} \tag{12}$$

2.3. Calculation Method for Blade Strength

The methodology employed for propeller strength calculation relies on finite element analysis based on elastic theory, which allows for the evaluation of stress and deformation characteristics of the blade. In this study, the finite element software ABAQUS 2023 is employed for conducting the blade strength calculations. The process begins with the geometric modeling of both the propeller and its hub, followed by importing and meshing in the finite element software. The surface pressure and wall shear stress on the propeller, obtained from the flow field, are then applied simultaneously. The deformation caused by the propeller blades is transferred to the fluid mesh. Hinge constraints are utilized to establish the connection relationship, and a fixed rotation speed is assigned to the propeller. Additionally, the material and cell properties of the propeller are defined. During the calculation, the hydrodynamic force load and centrifugal force load experienced by the propeller during operation are considered. The hydrodynamic load is determined through numerical calculation methods. The primary processing approach involves real-time loading of surface pressure and wall shear stress, calculated from the fluid grid, onto the structural grid of the propeller. Figure 1 provides an illustration of the blade strength calculation process.

2.4. Calculation Method for Fatigue Strength of Blade

The approach used to determine the fatigue strength of a propeller is based on the principles of material mechanics related to fatigue. The durability limit of the propeller blade under current working conditions is determined by combining the linear cumulative damage of the material with its material life curve. For a specific material subjected to a fatigue test at a defined cyclic characteristic R (a ratio of minimum stress to maximum stress), an *S-N* curve can be derived. This curve illustrates the relationship between the stress range (S) experienced during alternating stress and the number of stress cycles (N) required for failure under that specific stress. The *S-N* curve is a crucial aspect of fatigue research as it forms the basis for estimating fatigue limit and life. It is important to note that the *S-N* curve of a material changes with variations in the cyclic characteristic R. According to the linear cumulative damage theory, the fatigue damage of a component accumulates in a linear manner when subjected to alternating loads. The damage caused by different stress levels is considered independent and unrelated. Once the cumulative damage surpasses a critical threshold, fatigue occurs in the component.

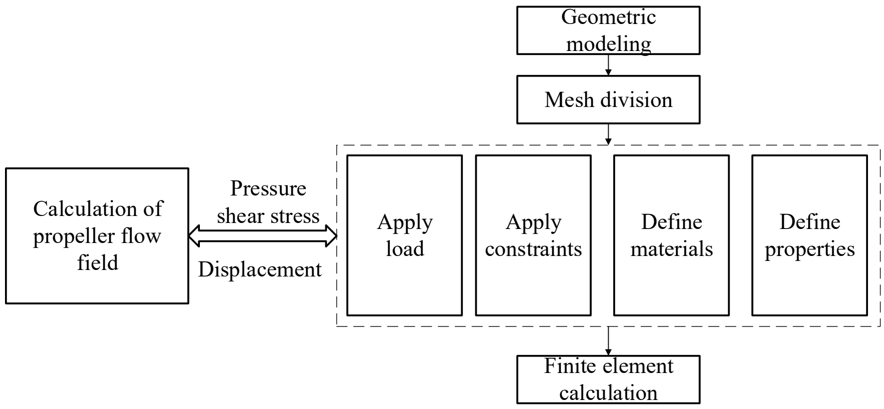

Figure 1. Blade strength calculation process.

To perform the fatigue strength analysis of the propeller, a finite element fatigue simulation is carried out using the software Fe-Safe 2023. Before initiating the calculation, it is imperative to identify the most critical point on the blade and monitor its stress state over time. By analyzing the stress variations at this critical point, the stress cycle and the corresponding number of cycles are extracted to assess the fatigue damage level of the material. Figure 2 illustrates the procedural steps involved in the calculation process of the blade fatigue strength.

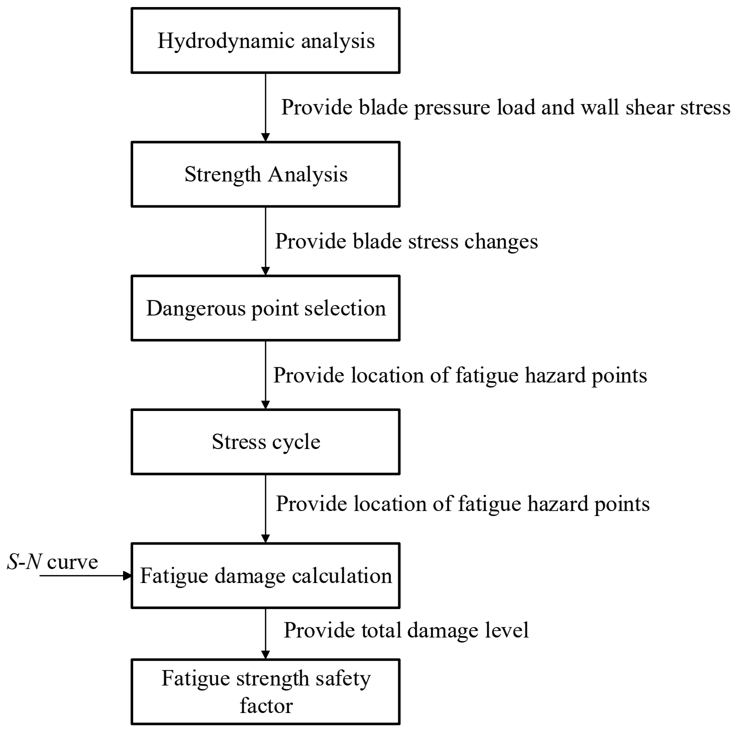

Figure 2. Procedural steps in blade fatigue strength calculation process.

3. Numerical Method

3.1. Description of the Model

The KP957 propeller is taken as the research object, since the cavitation results of the propeller are observed by HANJUN Shipbuilding Co. Ltd. (Busan, Republic of Korea) [24]. Cavitation simulations are carried out on the KP957 propeller, and the results are compared with experimental data [24] to validate the viability of the numerical simulation. The visual representation of the KP957 propeller model is depicted in Figure 3, with key parameters detailed in Table 1.

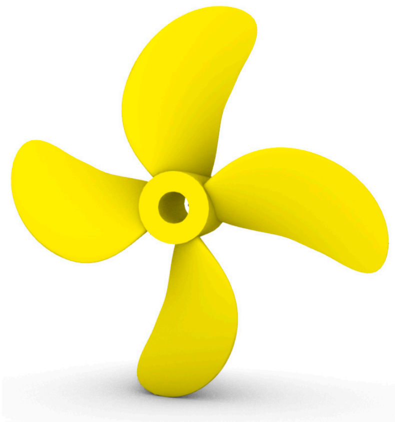

Figure 3. Geometry of the KP957 propeller.

Table 1. KP957 propeller main parameters.

Parameter	Value	Parameter	Value
Diameter (m)	0.2500	Skew angle (deg)	21.00
Expanded blade area ratio	0.4856	Hub-diameter	0.17
Propeller pitch ratio (0.7R)	0.7473	Number of blades	4

3.2. Mesh Generation

In this study, the computational domain is set up as a rectangular space with specific boundary conditions. The left side of the domain is designated as the velocity inlet, the right side as the pressure outlet, the cylindrical surface as the symmetric plane, and the propeller surface as the wall boundary. To mitigate the impact of reflected waves, the velocity inlet and pressure outlet boundaries are positioned at a considerable distance from the center of the propeller disk, specifically at 0.5 m and 2.1 m, respectively. The dimensions of the computational domain are set at 0.6 m in height and width. Additionally, to effectively capture vortex cavitation at the propeller tip, the computational domain is divided into two regions: the far-field stationary region and the near-field rotating region. The far-field region adopts a structured mesh, while the rotating region utilizes a polyhedral mesh. The near-field rotating domain is configured as a cylindrical shape with a diameter of 1.5 D and a length of 0.8 D (D represents the propeller diameter). In the tip-vortex area, a helical tube geometry with a diameter of 15 mm is introduced, extending from the propeller blade tip throughout the entire rotating region. To ensure accurate data transfer between the stationary and rotating regions and minimize errors, a prismatic layer mesh with a consistent mesh size is applied on both sides of the interface. The dimensions of the computational domain and the settings for boundary conditions are depicted in Figure 4, while the mesh division is presented in Figure 5.

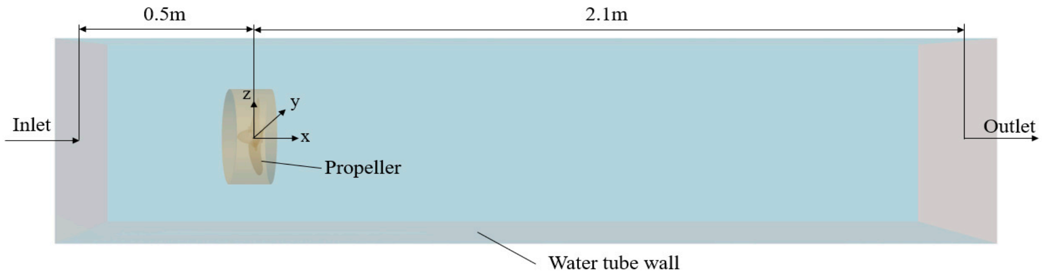

Figure 4. Schematic diagram of computational domain and boundary conditions.

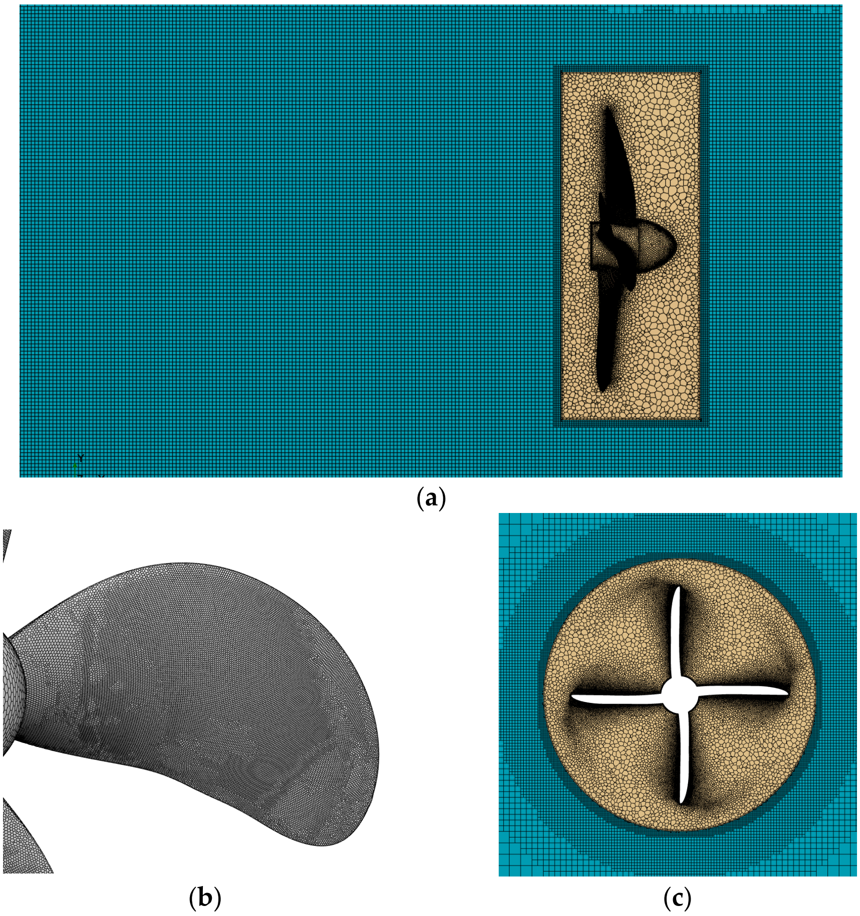

Figure 5. Schematic diagram of grid division. (**a**) Section $Y = 0$. (**b**) Blade mesh. (**c**) Section $X = 0$.

3.3. The Mesh Independence

In the mesh independence study, three meshes are chosen, as shown in Table 2. A structural mesh is used for the stationary domain and an unstructured hexahedral mesh is used for the rotational domain. The same mesh topology is employed in these three meshes, and the mesh refinement ratio is $\sqrt{2}$.

Table 2. Three meshes for mesh independence study.

Designation	Stationary Domain Mesh	Rotational Domain Mesh	The Total Number of Meshes
G_1	9,242,892	3,073,096	12,315,988
G_2	3,563,840	1,559,078	5,122,918
G_3	1,422,660	729,315	2,151,975

The impact of the propeller thrust coefficient K_T at J = 0.4607 is evaluated according to the ITTC recommended process [25], as shown in Table 3, where U_G is the grid uncertainty degree and R_G is the convergence ratio.

Table 3. Grid-independent analysis.

Designation	Simulated K_T	Test K_T	Deviation/%
G_1	0.1707	0.1677	1.79
G_2	0.1715	0.1677	2.27
G_3	0.1735	0.1677	3.46
R_G		0.4	
U_G		0.001067	
U_G (%G_1)		0.00625	

In Table 3, K_T predicted by the three sets of the grids are in good agreement with the experimental value [24]. R_G is greater than 0 but less than 1, indicating that the solution is monotonically convergent. The relative grid uncertainty U_G (%G_1) is 0.00625, which is small. The above results illustrate the reliability of the numerical simulation method in this paper. Considering the computation cost, G_2 grid is used to carry out the cavitation calculations in Section 4.

4. Results and Discussions

4.1. Validation

4.1.1. Performance of Cavitation-Free Propeller

The part calculates the performance of the cavitation-free propeller by setting the ambient pressure at 1 atmosphere. In the absence of cavitation, the thrust coefficients and torque coefficients of the propeller are evaluated across various advance coefficients, ranging from 0.1 to 0.8. Figure 6 illustrates the hydrodynamic performance and open water performance curves of the propeller at a speed of n = 15.5 r/s. The calculated thrust coefficient K_T, torque coefficient $10K_Q$, efficiency η_0 are found to be satisfactory against the corresponding experimental values [24].

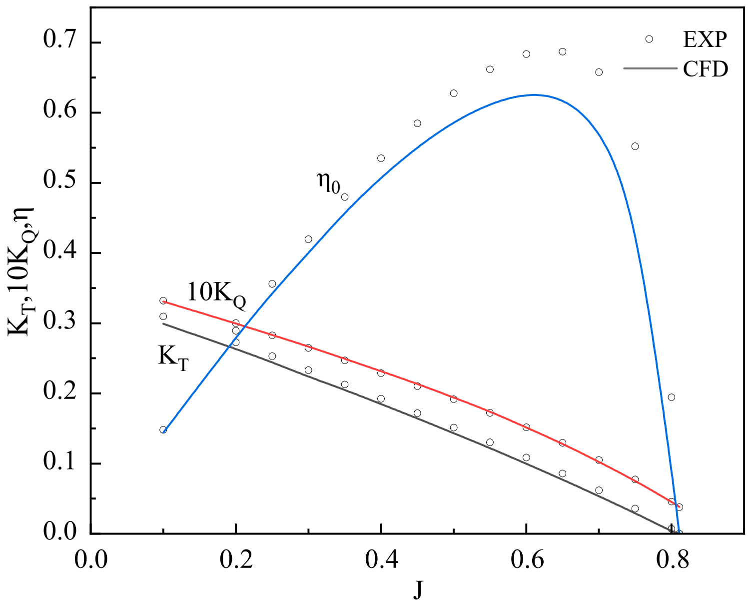

Figure 6. Comparison of the calculated propeller performance with the experimental data.

4.1.2. Cavitation Flow Field

The numerical calculation parameters used in the study are consistent with the test conditions outlined in reference [24]. These conditions include a wake field with a speed of 15.7 knots, a propeller rotational speed of n = 25 r/s, and a saturated vapor pressure of 3567 Pa. When observing the propeller from the rear, its position is at 0 degrees vertically upwards in the clockwise direction. Under these specific conditions, cavitation is formed.

The design draft wake distributions are reproduced inside the cavitation tunnel using a wake screen composed of brass wire meshes. The axial velocity at the surface of the propeller disk, as determined from the test measurements, is employed as the entrance velocity for the flow field. Figure 7 illustrates the contours of the simulated velocity entrance and the test axial velocity. It is observed that the largest difference between the velocity contour plots occurs in the 180° and 0° directions, and the velocities in other directions can effectively replicate the velocities measured in the experiment. The replicated velocity contour is then used as the velocity inlet, with the propeller speed set at n = 7.64 r/s (the self-propelled speed of 15.7 kn). The measured thrust coefficient error is found to be less than 5%, which meets the condition for using it as the velocity inlet.

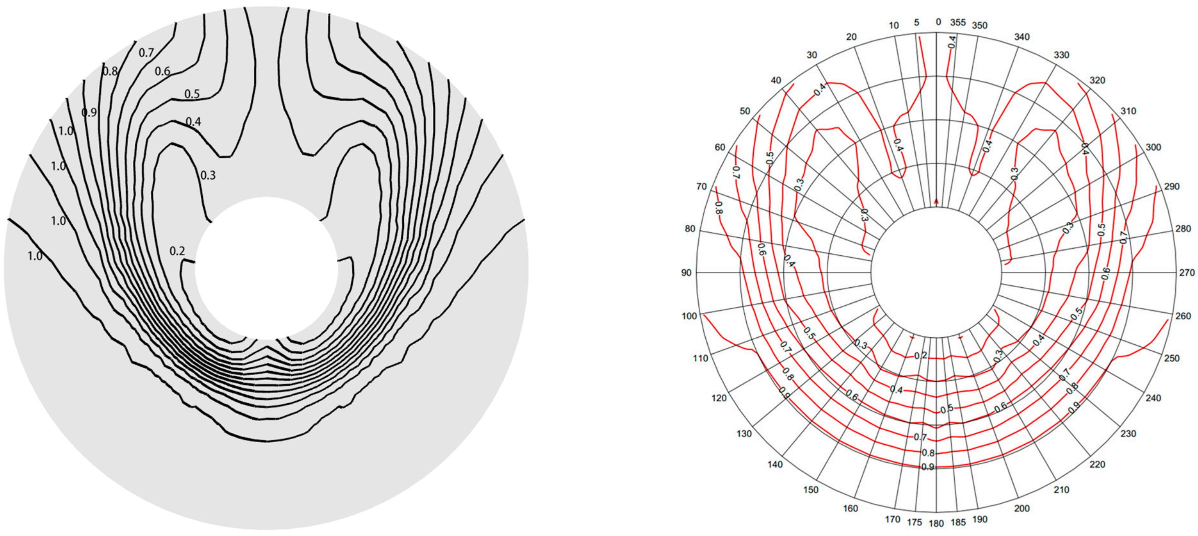

(**a**) (**b**)

Figure 7. Iso-axial velocity contours. (**a**) Simulation value. (**b**) Test value [24].

Once the stabilization of the non-cavitation flow field calculation is achieved, the Eulerian multiphase flow model and cavitation model are activated. The ambient pressure is adjusted to attain a cavitation number of 2.5553 at the rotational speed. To validate the accuracy of the numerical calculations, the cavitation morphology of the propeller blade at different phase angles is compared with the experimental results, as shown in Figure 8.

Isotropic surfaces are employed to depict the cavitation morphology of the propeller blade, which are defined by the volume fraction of gas-phase α, where $0 < \alpha < 1$. Figure 8 presents the entire process of cavitation growth and collapse of the propeller blade as it enters and exits the companion flow region. As the propeller blade enters the companion flow region, the blade back sheet cavitation firstly appears near the guide edge of the propeller blade. With the continued rotation of the propeller blade, the area of the blade back sheet cavitation gradually expands, and the tip vortex cavitation starts to emerge. The maximum blade back sheet cavitation area occurs at θ = 10°, followed by a gradual decrease in the cavitation area, as shown in Figure 8. Concurrently, the tip vortex cavitation intensifies. As the propeller blade gradually exits the companion flow region, the blade back sheet cavitation disappears, and the tip vortex weakens until it vanishes completely.

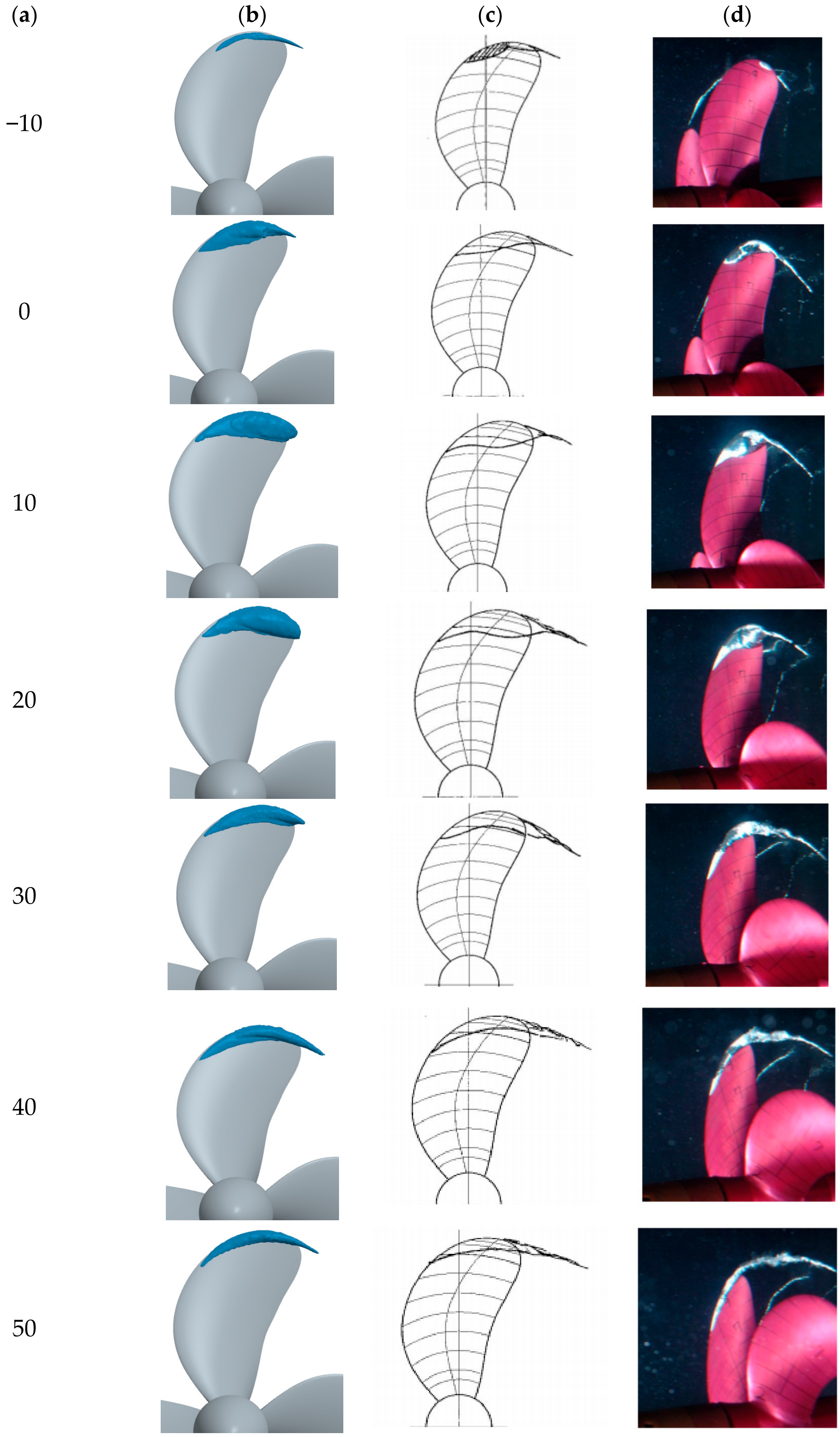

Figure 8. Comparisons of cavitation pattern between calculation results and test results observed at different θ values. (**a**) Circumferential Angle. (**b**) Calculation Results. (**c**) Test Depiction Diagram. (**d**) Test Photos [24].

The numerical calculations presented in Figure 8 precisely predict the progression of the cavitation process. The tip vortex cavitation at low circumferential angles is too small to be captured, while the tip vortex cavitation at high circumferential angles can be well captured. Although the denser mesh can better capture the tip vortex cavitation, it is not practical to re-mesh them considering the amount of the fluid-structure interaction calculations required. The observed phenomena, including blade cavitation initiation, blade cavitation area, tip vortex initiation, and tip vortex disappearance, align with the experimental results [24].

4.2. Cavitation Simulation with Different Vacuum Degrees

For large-load surface ship propellers, which are characterized by substantial sizes and high carrier speeds, numerical simulations and tests of model propeller cavitation are commonly conducted in depressurized cavitation water tanks. These experiments aim to simulate cavitation under different vacuum degrees by reducing the ambient pressure. Figures 9 and 10 depict the cavitation extent of the propeller at advance coefficients J = 0.4 and 0.5, with cavitation numbers ranging from 1.25 to 3. The figures reveal that a smaller cavitation number makes cavitation occurrence more likely for the same advance coefficient. Conversely, when the cavitation number is constant, larger propeller load results in more severe cavitation. In other words, with a constant propeller rotate speed, decreasing the speed and reducing the advance coefficient make cavitation more likely to occur. This observation highlights that when the carrier propeller initiates high-speed operation, cavitation is prone to happen.

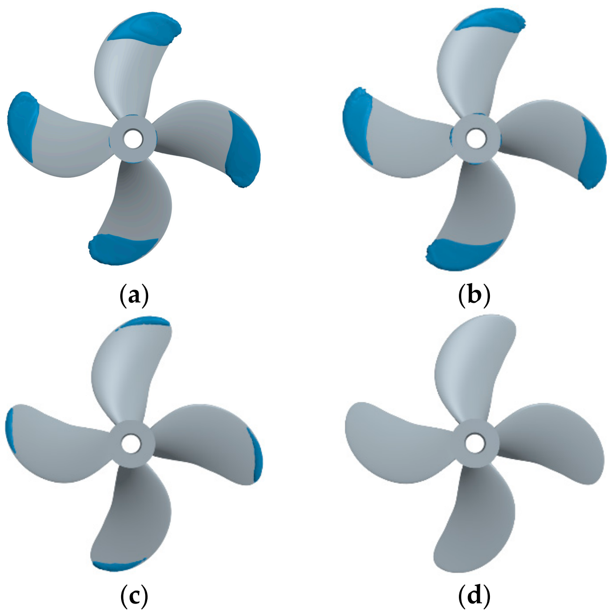

Figure 9. Cavitation cloud diagram of the propeller at advance coefficient J = 0.4. (**a**) $\sigma_n = 1.25$. (**b**) $\sigma_n = 1.5$. (**c**) $\sigma_n = 2$. (**d**) $\sigma_n = 3$.

4.3. Effect of Cavitation on Propeller Performance

The cavitation phenomenon associated with the propeller can be divided into two stages: the first and the second stage. In Figure 11, the hydrodynamic performance for the KP957 propeller model under cavitation is presented, maintaining a constant number of advance coefficient for the propeller while systematically varying the cavition number. The horizontal axis in the figure represents the cavitation number, while the vertical axis represents the values of K_T, $10K_Q$, η_0. As evident from Figure 11a, as $\sigma_n > 1.5$, the propeller blade exhibits the presence of cavitation, and the values of K_T, $10K_Q$, η_0 remain relatively unchanged with the cavitation number. This indicates that the performance of the propeller is similar to the case when no cavitation is present, representing the first stage of cavitation.

Conversely, as $\sigma_n < 1.5$, there is a sharp decrease in the values of K_T, $10K_Q$, η_0, and the area covered by cavitation on the propeller increases. This scenario is typically referred to as the second stage of cavitation. Figure 11 shows that there is always a polarization zone in the cavitation performance of the propeller under a constant advance coefficient.

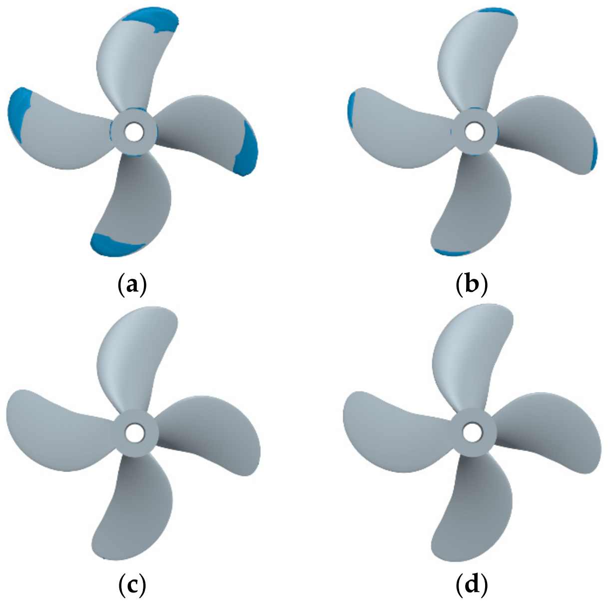

Figure 10. Cavitation cloud diagram of the propeller at advance coefficient J = 0.5. (**a**) $\sigma_n = 1.25$. (**b**) $\sigma_n = 1.5$. (**c**) $\sigma_n = 2$. (**d**) $\sigma_n = 3$.

Cavitation typically undergoes three stages: inception, growth, and collapse. Due to its pronounced unsteady characteristics, especially during the cavitation collapse stage, intense local pressure pulsations occur, leading to a significant increase in noise and vibration. The cavitation collapse at the structure boundary also exerts a substantial erosive effect on the material. As the propeller rotates, numerous transient cavitations in the blade area collapse and rebound, causing localized increases in blade surface pressure, resulting in blade vibration. Figures 12 and 13 illustrate stress and strain diagrams during propeller rotations with the advance coefficients J = 0.4 and 0.5.

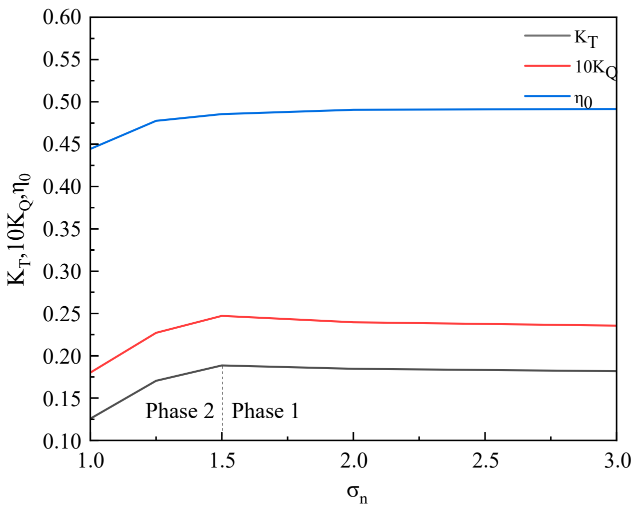

(**a**)

Figure 11. *Cont.*

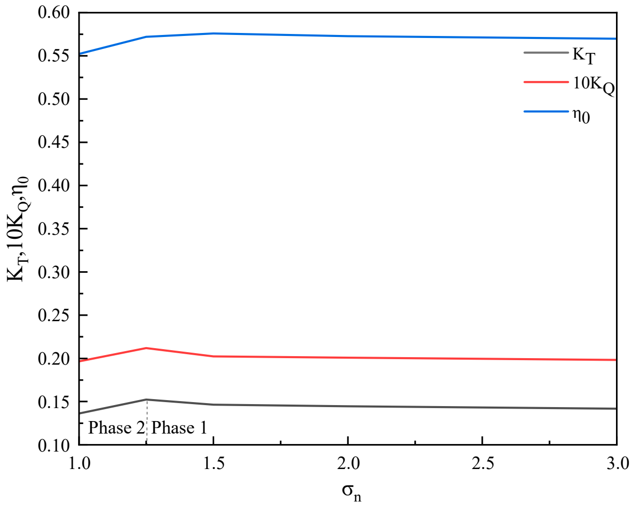

(**b**)

Figure 11. The effect of cavitation on propeller performance. (**a**) J = 0.4. (**b**) J = 0.5.

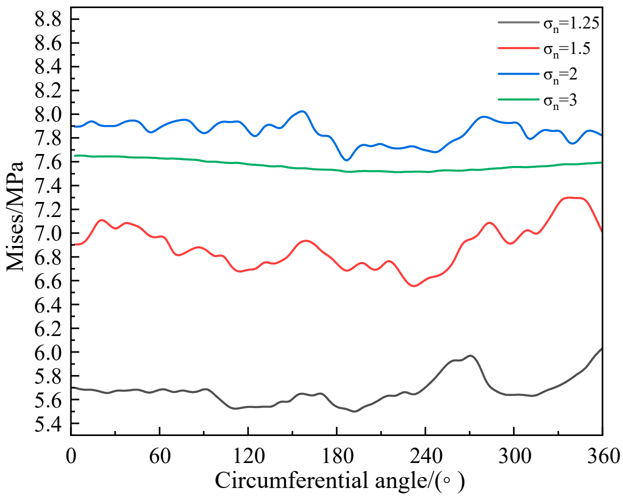

(**a**)

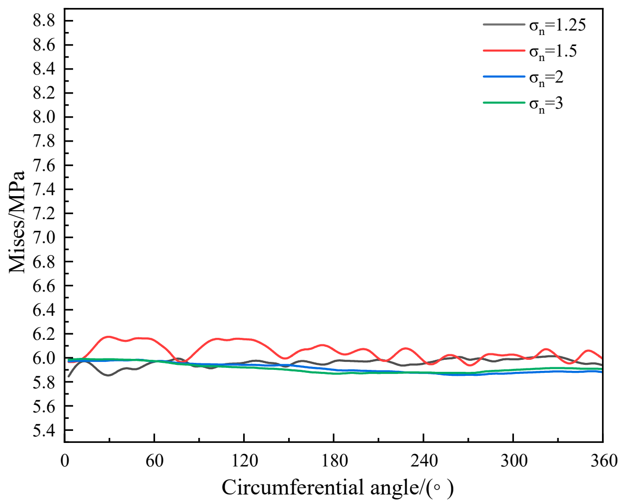

(**b**)

Figure 12. Variations of Mises during one propeller rotation. (**a**) J = 0.4. (**b**) J = 0.5.

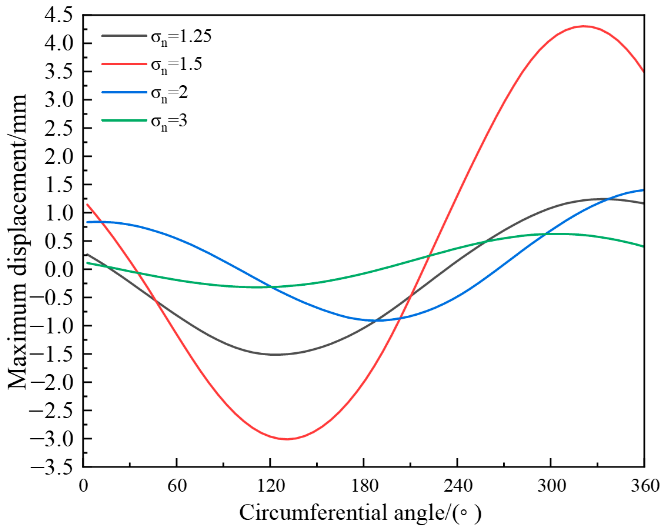

(**a**)

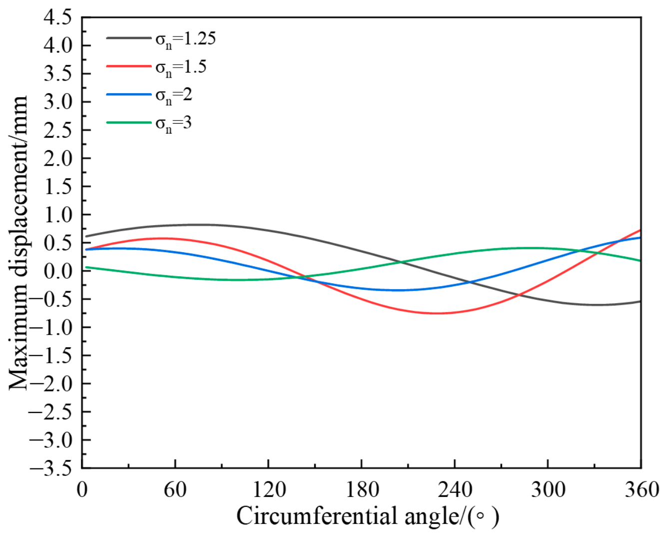

(**b**)

Figure 13. Variations of True strain during one propeller rotation. (**a**) $J = 0.4$. (**b**) $J = 0.5$.

In the initial stage, depicted in Figure 13, as the cavitation number decreases, the vibration amplitude of the propeller blades notably diminishes. This is attributed to the larger cavitation coverage area, which extends from the leading edge of the blade tangent surface to beyond the trailing edge without breaking on the blade, causing uneven stress. Apparently, an increased cavitation area results in a decline in propeller performance. In the second stage, the blade's vibration amplitude gradually becomes gentler as the cavitation area decreases with an increasing number of cavitations, reducing the impact area on the blade caused by cavitation rupture. When cavitation disappears, the strain curve of the blade approximates a straight line.

As shown in Figure 12, the blade strain during one rotation becomes gentler upon increasing the advance coefficient. This is because a higher advance coefficient leads to a reduced cavitation bubble area, which lessens the impact of cavitation on the blades. By appropriately increasing the propeller advance speed, it is possible to mitigate the impact of cavitation and weaken vibration to some extent.

Cavitation implosion impacts the propeller blade, resulting in material erosion and breakage. As depicted in Figure 12, when cavitation is in the second stage, the average stress on the propeller is relatively high, and the stress curve fluctuates significantly during one rotation, signifying the impact of cavitation on the blade. It is only when cavitation completely disappears that the stress curve becomes flat. When the advance coefficient is 0.4 and 0.5, the vibration at the boundary point is maximum. Referring to the strain curve in Figure 12, the strain curve fluctuates most severely under the corresponding number of bubbles.

After increasing the advance coefficient as shown in Figure 12, the strain curve of the blade becomes smoother within one revolution. This is due to the decrease in bubble area and the reduced impact of cavitation on the blades as the advance coefficient increases. By properly increasing the propeller speed, it is possible to not only reduce the influence of cavitation, but also reduce vibration to a certain extent.

By comparing Figures 12 and 13a,b, it is evident that parameters such as stress, maximum displacement, and thrust coefficient decrease with an increase in advance coefficient. This is caused by the reduction in cavitation area resulting from the increased advance coefficient. In addition, the stress and maximum displacement in Figures 12 and 13 do not increase with an increase in the number of cavitations. This is because when the number of cavitations is below the critical point, the blade is basically covered by the cavitations, and the cavitation collapse primarily occurs at the trailing edge. As a result, the maximum displacement and stress on the blade remain relatively small. However, when the number of cavitations exceeds the critical point, the majority of the impact load generated by the cavitation collapse acts on the blade, leading to larger maximum displacement and stress. Nevertheless, as the number of cavitations continues to increase, the area of cavitation decreases, which causes the blade displacement and stress to decrease as well.

In the initial stage, cavitation has no effect on the hydrodynamics performance, but the blade is subject to irregular impact loads. In the second stage, the impact load on the blade is lessened, but it still affects the hydrodynamic performance of the propeller.

4.4. Intensity Calculations

The finite element analysis is based on the software Abaqus 2023 for preprocessing of the propeller blades under consideration. The structural configuration chosen is that of a semi-immersed propeller single blade connected to the propeller hub. The material properties of the blade are defined as follows: the density ρ = 2800 kg/m^3, Young's modulus E = 70.8 GPa, and Poisson's ratio σ = 0.33. These material property parameters are set as the model material properties. The blades are connected to the propeller hub via articulation about beams on the inner hole of the hub, with the direction aligned with the propeller axis. A centrifugal force load is applied to the blade surface at a specified speed of 15.5 r/s.

Figure 14 presents the stress cloud of the blade at 0° for different cavitation numbers (1.25, 1.5, 2, and 3). As the cavitation number increases, the low-stress zone at the tip of the leaf blade proportionally diminishes, and the stress distribution at the root becomes more uniform. The initiation of cavitation induces a localized high-stress phenomenon at both the back and the root of the blade surface, gradually diminishing with the increasing numbers of cavitation. Propeller cavitation also leads to elevated local stresses at the root of the blade, which, in extreme cases, can result in the breakage of the propeller blade. Hence, it is imperative for propellers to minimize cavitation effects.

4.5. Fatigue Strength Calculations

In the fatigue analysis module, the *S-N* curve is essential for calculating fatigue strength. Figure 15 presents the *S-N* curve for the aluminum alloy (AL2024T4) propeller material. Notably, the propeller experiences significant variation in surface load during its 360° rotation cycle, featuring multiple cyclic characteristics. Identifying the node near 0.7R of the blade's trailing edge with the maximum stress change amplitude as the critical node, calculations are performed for stress distribution at 144 phases, each 2.5° apart, throughout the rotational position of the blade. The stress cyclic characteristics of the blade are extracted at 2.5° intervals, as illustrated in Figure 12.

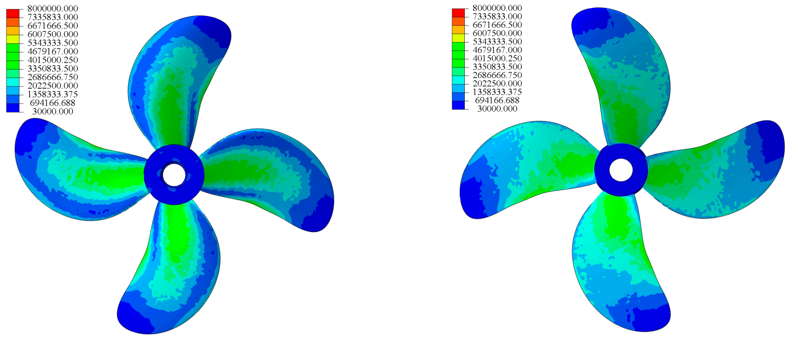

(**a**)

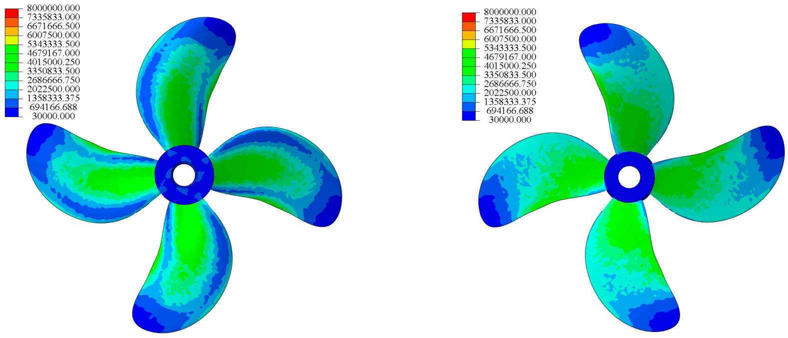

(**b**)

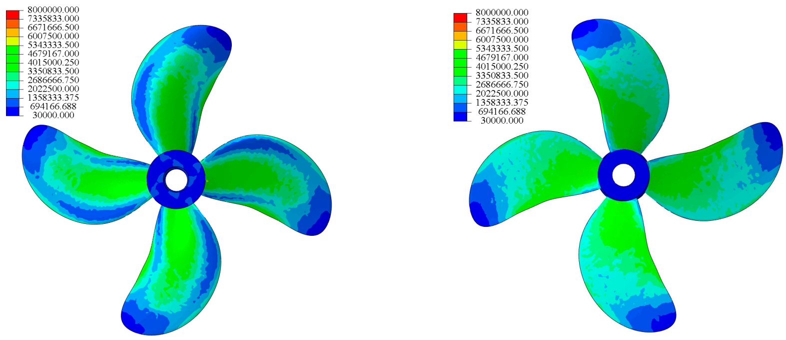

(**c**)

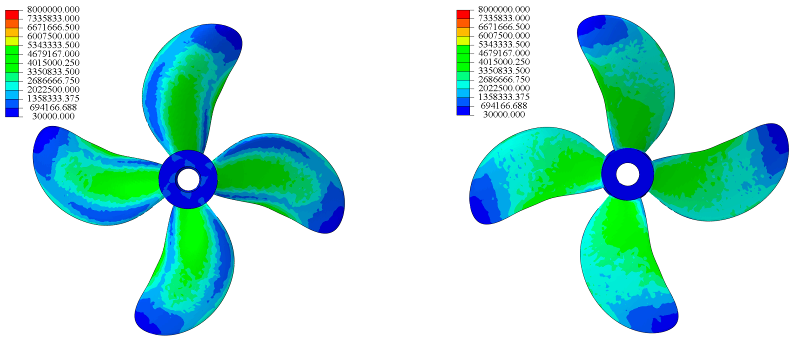

(**d**)

Figure 14. Propeller stress contours with different cavitation numbers. (**a**) $\sigma_n = 1.25$. (**b**) $\sigma_n = 1.5$. (**c**) $\sigma_n = 1.5$. (**d**) $\sigma_n = 3$.

Figure 15 displays the *S-N* curve for the aluminum alloy material. Due to the low stress induced by the propeller mold, it is considered that this load does not pose a structural damage risk when the number of cycles exceeds 10^7. Therefore, stress amplification is necessary before conducting fatigue calculations to further investigate its inherent behavior. By multiplying the stress on the propeller blades with a coefficient capable of inducing fatigue damage to the blade, as long as this factor satisfies the criteria for propeller fatigue damage.

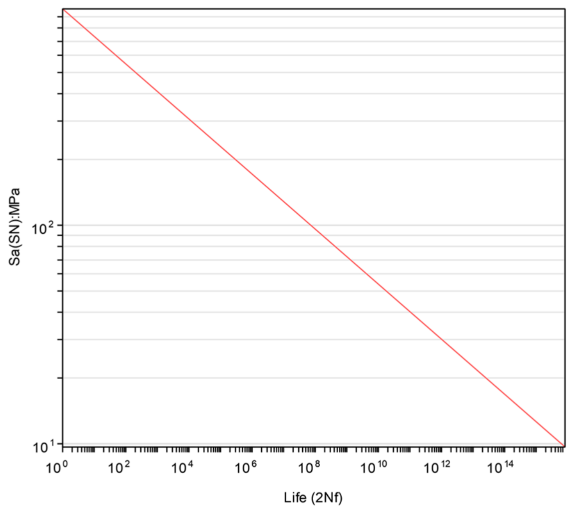

Figure 15. *S-N* curve.

Figure 16 depicts the results of fatigue life calculations for different cavitation numbers with stress amplification by a factor of 50 for the advance coefficient J = 0.4. The blade life curve exhibits a sharp rise when $\sigma_n < 1.5$, indicating the presence of a substantial cavitation area, commonly referred to as a super cavitation flow. Although the blade life is prolonged, the propulsion performance of the propeller is significantly affected. As $\sigma_n > 1.5$, the blade life curve declines firstly and then rises as $\sigma_n > 2$. This behavior can be attributed to the propeller entering the second stage of cavitation, where cavitation not only induces blade cavitation but also irregular vibrations, resulting in a reduction in propeller life. The rise as $\sigma_n > 2$ is because the cavitation area decreases, and the impact of cavitation collapse on the blade is reduced. Consequently, the propeller blade experiences more stable oscillations in the second stage of cavitation.

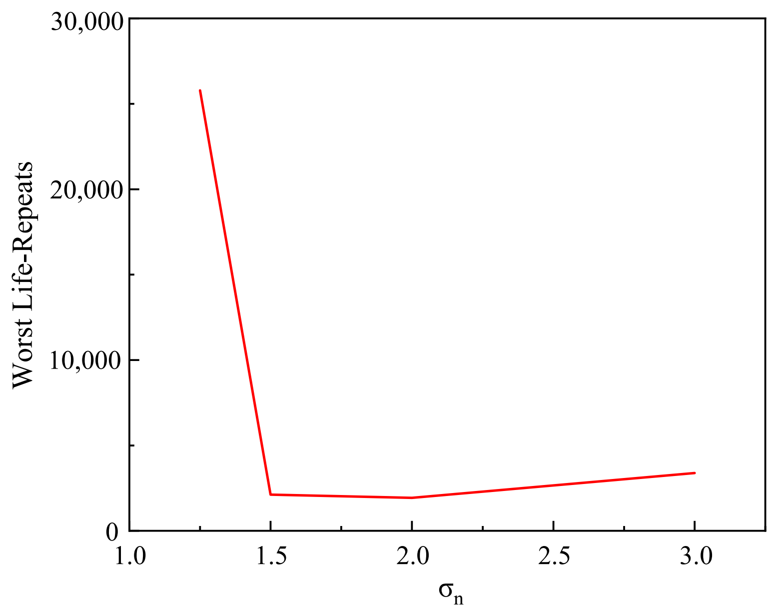

Figure 16. Worst Life-Repeats at different cavitation numbers.

Figure 17 presents the cloud diagram of blade life after cyclic loading, revealing that the majority of damage to the blade is concentrated at the root. The irregular generation and collapse of cavitation in the propeller blade create a non-constant load, resulting in irregular vibrations that can easily lead to blade fracture. The second stage of cavitation not only affects the propeller through cavitation but also induces cavitation due to the irregular vibration of the blade, resulting in a reduction in propeller life.

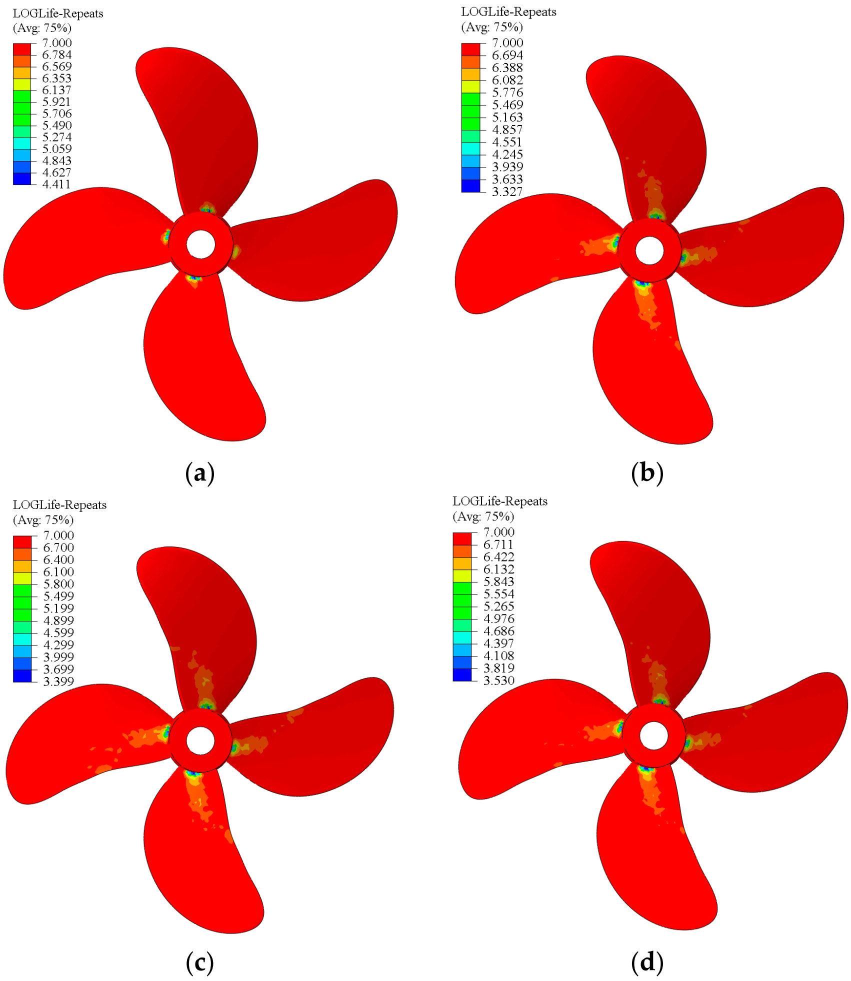

Figure 17. Propeller fatigue life. (**a**) $\sigma_n = 1.25$. (**b**) $\sigma_n = 1.5$. (**c**) $\sigma_n = 2$. (**d**) $\sigma_n = 3$.

5. Conclusions

This study employs a combination of Computational Fluid Dynamics (CFD) and Finite Element Methods (FEM) to examine the cavitation characteristics and fatigue strength of the KP957 propeller under axial uniform incoming flow conditions, yielding the following conclusions:

1. The cavitation's area and volume decrease progressively with an increase in the advance coefficient. Moreover, under the same advance coefficient, both the area and volume of the cavitation decrease as the number of cavitations increases.
2. With a consistent advance coefficient, the first cavitation stage has no impact on propeller performance but results in reduced blade life. Conversely, the second cavitation stage has almost no effect on blade life but diminishes the hydrodynamic performance of the propeller.
3. The vibration amplitude decreases with the increase of the advance coefficient, and the maximum vibration amplitude occurs at the critical point of cavitation.
4. Cavitation occurrence induces vibration in the propeller blade, posing a risk of damage to the blade root.

It is important to note that the fatigue analysis in this study solely considers the impact of stress on the blade and does not incorporate the influence of cavitation caused by cavitation. Consequently, the actual life of the propeller may be lower than predicted.

Additionally, the developed propeller strength analysis lacks consideration for the actual propeller size, and the enlarged factor in the fatigue analysis does not precisely predict the real propeller's life. Nonetheless, it effectively highlights the fatigue-prone areas of the propeller under cavitation bubbles.

Author Contributions: Methodology, X.Z., Q.X. and Z.X.; Calculation, X.Z., Q.X. and Z.X.; Investigation, X.Z., Q.X. and M.Z.; writing-original draft, Q.X.; writing-review & editing, X.Z. and M.Z.; financial support, X.Z. and M.Z.; checking and supervision, M.Z. All authors have read and agreed to the published version of the manuscript.

Funding: The work is sponsored by Shandong Province Natural Science Foundation ZR2022QE035, ZR2022QE106; Heilongjiang Province Natural Science Foundation LH2023E076, LH2023E075; the National Science Foundation of China 52301365.

Institutional Review Board Statement: Not applicable.

Informed Consent Statement: Not applicable.

Data Availability Statement: No data were used to support this study.

Acknowledgments: The authors express gratitude to Shandong Province Natural Science Foundation; Heilongjiang Province Natural Science Foundation; the National Science Foundation of China.

Conflicts of Interest: The authors declare no conflict of interest.

References

1. Haeji, J.; Jungsik, C. Experimental Study of Cavitation Damage to Marine Propellers Based on the Rotational Speed in the Coastal Waters. *Machines* **2022**, *10*, 793.
2. Tadros, M.; Ventura, M.; Soares, C.G. Effect of Hull and Propeller Roughness during the Assessment of Ship Fuel Consumption. *J. Mar. Sci. Eng.* **2023**, *11*, 040784. [CrossRef]
3. Ehsan, C.N.; Faysal, H.M.; Mashud, K.M.; Islam, R.; Bhuiyan, A.A. Numerical Investigation for Mitigation of Cavitation in High-Speed Marine Propeller Using Mass Injection Approach Journal. *Iran. J. Sci. Technol.* **2023**, *47*, 1693–1709.
4. Long, Y.; Long, X.; Ji, B.; Huang, H. Numerical simulations of cavitating turbulent flow around a marine propeller behind the hull with analyses of the vorticity distribution and particle tracks. *Ocean. Eng.* **2019**, *189*, 106310. [CrossRef]
5. Paik, K.J.; Park, H.; Seo, J. URANS simulations of cavitation and hull pressure fluctuation for marine propeller with hull interaction. In Proceedings of the 3rd International Symposium on Marine Propulsors, Launceston, Tasmania, 5–8 May 2013; pp. 389–396.
6. Yilmaz, N.; Aktas, B.; Sezen, S.; Atlar, M.; Fitzsimmons, P.; Felli, M. Numerical investigations of propeller-rudder-hull interaction in the presence of tip vortex cavitation. In Proceedings of the 6th Symposium on Marine Propulsors, SMP'19, Rome, Italy, 16–20 May 2019; pp. 407–413.
7. Rizk, M.A.; Belhenniche, S.E.; Imine, O.; Kinaci, O.A. Numerical Investigation for Mitigation of Cavitation and Its Performance Behind a Generic Hull. *J. Mar. Sci. Appl.* **2023**, *22*, 273–283. [CrossRef]
8. Zheng, C.S. The numerical prediction and analysis of propeller cavitation benchmark tests of YUPENG ship model. *J. Mar. Sci. Eng.* **2019**, *7*, 387. [CrossRef]
9. Lloyd, T.; Vaz, G.; Rijpkema, D.; Reverberi, A. Computational fluid dynamics prediction of marine propeller cavitation including solution verification. In Proceedings of the Fifth International Symposium on Marine Propulsors, Smp17, Espoo, Finland, 12 June 2017.
10. Zhang, L.; Ye, J. Cavitation impact damage of polymer: A multi-physics approach incorporating phase-field. *Comput. Methods Appl. Mech. Eng.* **2023**, *417*, 116420. [CrossRef]
11. Ortolani, F.; Dubbioso, G.; Muscari, R.; Mauro, S.; Di Mascio, A. Experimental and numerical investigation of propeller loads in off-design conditions. *Mar. Sci. Eng.* **2018**, *6*, 45. [CrossRef]
12. Rusinov, P.O.; Blednova, Z.M. Improving the Longevity of the Propellers by the TiNiCo-B4C-Co Intelligent Surface Compositions Operating at Low Temperatures. *Mater. Sci. Forum* **2018**, *4554*, 39–43. [CrossRef]
13. Nasiri, S.; Parniani, M.; Saeed, P. A multi-objective optimal power management strategy for enhancement of battery and propellers lifespan in all-electric ships. *J. Energy Storage* **2023**, *65*, 107183. [CrossRef]
14. Arvind, K.; Nikhil, B.; Subhamoy, S.; Sen, S. Reliability analysis of 15MW horizontal axis wind turbine rotor blades using fluid-structure interaction simulation and adaptive kriging model. *Ocean Eng.* **2023**, *288*, 116138.
15. Hu, J.; Li, X.; Zhu, J.; Ning, X.; Wan, Q.; Lin, C. Effect of cavitation on fluid-structure interaction of a cantilever hydrofoil. *Ocean Eng.* **2023**, *288*, 116025. [CrossRef]
16. Lou, B.; Cui, H. Fluid–Structure Interaction Vibration Experiments and Numerical Verification of a Real Marine Propeller. *Pol. Marit. Res.* **2021**, *28*, 61–75. [CrossRef]

17. Xiao, X.; Volodymyr, O.; Donald, M. High cycle fatigue life assessment of notched components with induced compressive residual stress. *Int. J. Press. Vessel. Pip.* **2023**, *206*, 105069. [CrossRef]
18. Magoga Teresa, M.; Seref, A.; Karl, S. Implementation of a nominal stress approach for the fatigue assessment of aluminium naval ships. *Procedia Struct. Integr.* **2023**, *45*, 28–35. [CrossRef]
19. Yang, L.; Yang, B.; Yang, G.; Jiang, L.; Xiao, S.; Zhu, T. Fatigue evaluation method based on equivalent structural stress approach for bolted connections. *Int. J. Fatigue* **2023**, *174*, 107738. [CrossRef]
20. Thambi, J.; Tetzlaff, U.; Schiessl, A.; Lang, K.-D.; Waltz, M. Evaluation of the relationship between stress and lifetime of Pb-free solder joints subjected to vibration load using a generalized local stress approach. *Microelectron. Reliab.* **2020**, *106*, 113560. [CrossRef]
21. Wang, J.; Zeng, D.; Lu, L. Fatigue life evaluation for ring-welded lap joints of stainless steel based on fracture mechanics approach. *Theor. Appl. Fract. Mech.* **2023**, *127*, 104067. [CrossRef]
22. Vijayanandh, R.; Venkatesan, K.; Kumar, M.S.; Kumar, G.R.; Jagadeeshwaran, P.; Kumar, R.R. Comparative fatigue life estimations of Marine Propeller by using FSI. *J. Phys. Conf. Ser.* **2020**, *1473*, 012018. [CrossRef]
23. Giorgi, M.; Ficarella, A.; Fontanarosa, D. Implementation and validation of an extended Schnerr-Sauer cavitation model for non-isothermal flows in OpenFOAM. *Energy Procedia* **2017**, *126*, 58–65. [CrossRef]
24. HANJUN Shipbuilding Co., Ltd. *Hull Form Study for HANJUN DWT 160,000 Ton Crude Oil Tanker*; Moeri Model Test Report; HANJUN Shipbuilding Co., Ltd.: Busan, Republic of Korea, 2010.
25. ITTC. *CFD General Uncertainty Analysis in CFD Verification and Validation Methodology and Procedures (7.5-03-01-01)*; Revision 01; ITTC Recommended Procedures and Guidelines; ITTC: Ayutthaya, Thailand, 2002.